Tunable magnetic anisotropy in two-dimensional CrX_3/AlN (X = I, Br, Cl) heterostructures

Haiyan Zhu,[1] Yifan Gao,[1] Yusheng Hou,[2] Zhigang Gui,[1,3,*] and Li Huang[1,†]

[1]*Department of Physics, Southern University of Science and Technology, Shenzhen, Guangdong 518055, China*

[2]*Guangdong Provincial Key Laboratory of Magnetoelectric Physics and Devices, Center for Neutron Science and Technology, School of Physics, Sun Yat-Sen University, Guangzhou, 510275, China*

[3]*Academy for Advanced Interdisciplinary Studies, Southern University of Science and Technology, Shenzhen 518055, China*

(Received 4 May 2022; revised 1 August 2022; accepted 30 September 2022; published 12 October 2022)

Controlling the magnetic anisotropy of two-dimensional (2D) ferromagnets (FMs) is of great importance for the development of next generation spintronics. Here, by combining the 2D FM chromium trihalides CrX_3 (X = I, Br, Cl) monolayer (ML) with the fully hydrogenated bilayer AlN (AlN-2L) together, the electronic and magnetic properties, especially the magnetic anisotropies, of CrX_3/AlN heterostructures (CrX_3 HSs) are systematically investigated based on first-principles calculations. When the polarization direction of AlN-2L reverses, the magnetic easy axis of CrX_3 MLs can be switched between out-of-plane and in-plane directions. Particularly the magnetic anisotropic energy is tuned by a maximum of 200% variation in CrI_3/AlN. It is shown that the different effects of AlN-2L on the modulation of the magnetic easy axis of CrX_3 MLs are related to their different interfacial charge transfer/redistribution across their interfaces. In addition, a transition from FM semiconductor to half-metal is found in all CrX_3 MLs when the polarization direction points toward CrX_3 MLs. Our results suggest a feasible avenue for the design of van der Waals HSs to realize the control of magnetic anisotropy in 2D FMs.

DOI: 10.1103/PhysRevB.106.134412

I. INTRODUCTION

The discovery of intrinsic ferromagnetism in two-dimensional (2D) materials, including the currently intensively investigated CrI_3 [1], $Cr_2Ge_2Te_6$ [2], and Fe_3GeTe_2 [3], have incited great interest in 2D magnets. According to the Mermin-Wagner theory [4] based on the isotropic Heisenberg model, finite-temperature long-range magnetic order in 2D magnetic materials was believed to be impossible due to the thermal fluctuation of magnetic moments. To counteract such thermal fluctuation in 2D magnetic materials, magnetocrystalline anisotropy (MCA) is required as one of the most important properties by opening a magnon gap [2,5]. Compared with the magnetic thin films grown by conventional methods, 2D van der Waals (vdW) magnets with large MCA and high Curie temperature (T_C) are desirable for practical applications in high-density magnetic memories and magnetic tunnel junctions [6–9].

As a representative type of 2D ferromagnetic (FM) materials, the magnetic properties of a CrX_3 (X = I, Br, Cl) monolayer (ML) have been intensively studied. Experimental results show a FM ground state with an out-of-plane magnetic easy axis for CrI_3 and $CrBr_3$ and an in-plane easy axis for $CrCl_3$ [10,11], and T_C values decrease as the halogen element changes from I to Cl, ∼45 K for CrI_3 [1], ∼34 K for $CrBr_3$ [12], and ∼17 K for $CrCl_3$ (bulk) [13]. Significant efforts have been devoted to promoting the magnetic properties of a CrX_3 (X = I, Br, Cl) ML. For example, 47% enhanced magnetic anisotropy in a CrI_3 ML was reported when a 5% compressive strain was applied [14]. Furthermore, alloying CrI_3 [15] and a $CrCl_3$ ML [16] with isovalent W atoms has been proposed to significantly enhance the FM coupling in these two 2D semiconductors. Experimentally, chemical adsorption, electric field, and pressure were also reported to tune their electronic and magnetic properties in CrX_3 [17–22]. Among various approaches, vdW heterostructures (HSs) formed by integrating a 2D magnetic material with a polar or nonpolar nonmagnetic material are widely considered as highly promising strategies to substantially enrich their functionalities and improve their properties for spintronics applications [23–30]. As reported by Zhao *et al.* [26], the semiconducting nature of CrI_3 changes to half-metallic in the CrI_3/Sc_2CO_2 HSs when the polarization direction of the Sc_2CO_2 layer points to the CrI_3 layer. Meanwhile, it has been shown that electrostatic doping into 2D magnetic materials can tune their MCA [18,31–34]. Especially the intrinsic polarization of 2D polar or ferroelectric (FE) layers in vdW HSs can give rise to similar effects, and it is switchable as well. Therefore, it is quite interesting and of practical significance to examine the possibility of realizing the control/optimization of the MCA of 2D magnetic materials by proximity with a polar or FE layer. Although authors of previous works have reported nonvolatile electrical control of 2D FMs by interfacing with intrinsic polarized substrates in vdW HSs [23,25,28,30], the detailed physical origin of how MCA of the constituent 2D magnetic layers changes with proximity to the FE/polar layers requires further exploration. First, which is the key factor, such as interfacial structural modification and charge

*guizg@sustech.edu.cn
†huangl@sustech.edu.cn

transfer/redistribution, and how do these factors tune MCA? More importantly, what are the requirements for the FE/polar layers in the vdW HSs for an effective tuning of magnetic properties of the magnetic layer, particularly to enhance its MCA?

On the other hand, as one of the 2D semiconductors with potential device applications, atomically thin AlN nanosheets with both wurtzite (WZ) and graphitic structure have been extensively studied [35–39]. It is noted that the atomically thin AlN nanosheets in the WZ phase are stable down to one or two layers with fully hydrogenated surfaces [40,41], which present strong intrinsic polarization along the out-of-plane direction due to the lack of inversion symmetry. It has also been reported that the polarization of ultrathin films with the same WZ structure (e.g., ZnO) can be switched under moderate electric field [42]. The 2D AlN with the WZ structure can thus be a good candidate as the polar layer in a vdW HS to explore its role in tuning the magnetic properties in CrX_3 MLs.

In this paper, we systematically investigate the electronic and magnetic properties, especially the magnetic anisotropies of the type of 2D vdW HSs consisting of a CrX_3 ML and a hydrogenated bilayer (2L) AlN by using first-principles calculations. Our results show that the MCA of all CrX_3 MLs exhibit strong dependence on the polarization direction of the constituent polar layer. The magnetic easy axis of CrI_3 is switchable in the opposite polarization of the AlN layer, giving rise to a large variation of MCA (up to 2115 μeV/Cr). The physical origin of the tunable MCA and the enhanced FM couplings in CrX_3 MLs are closely related to the different interfacial charge transfer and redistribution induced by the polarization of the AlN layer in these HSs. In this paper, we not only demonstrate a feasible avenue to reversibly control the magnetic anisotropy of the 2D FM CrX_3 MLs but also gain deep physical insight into understanding the coupling between FE and magnetic layers in 2D vdW HSs.

In Sec. II, we present the methods used in this paper. In Sec. III, we report the electronic and magnetic properties of CrX_3 MLs and CrX_3/AlN HSs and discuss the origin of the tunable MCA in the HSs. Finally, a summary is given in Sec. IV.

II. COMPUTATIONAL DETAILS

The first-principles calculations are conducted within the density functional theory (DFT) framework using the projected augmented wave method as implemented in the Vienna *Ab initio* Simulation Package [43]. The exchange-correlation term is treated by the generalized-gradient approximation [44] of the Perdew-Burke-Ernzerhof functional [45]. The Kohn-Sham orbitals are expanded in a plane-wave basis set with an energy cutoff of 500 eV. The semicore states of Cr $3p$ are treated as valence electrons as well. An effective onsite Hubbard U adopted to treat the electron correlation for the localized d orbitals of Cr atoms is tested (see Supplemental Note 1 in the Supplemental Material [46]), and a value of 3.0 eV is chosen [16,24,47,48]. The structures are fully relaxed until the forces on each atom are < 0.01 eV/Å and the energy difference between two consecutive self-consistent steps is $<10^{-7}$ eV. Monkhorst-Pack meshes [49] with the reciprocal space resolution of $2\pi \times 0.025$ Å^{-1} ($2\pi \times 0.015$ Å^{-1}) are used to generate the k-point sampling in structural optimizations (the calculations of the electronic and magnetic properties). A vacuum space of 15 Å is adopted in the nonperiodic direction to avoid the interactions between adjacent images. The vdW interactions between the layers are described by the D2 Grimme method [50,51]. Tests have been done to make sure that all the results are converged with respect to energy cutoff, system size, and k-points sampling. The thermal stability of the preferable CrX_3 HSs is further examined by *ab initio* molecular dynamics simulations with the NVT canonical ensemble and Nose-Hoover thermostat algorithm. Using the finite difference method [52], the phonon dispersion spectrum is also obtained to determine the dynamic stability for $CrBr_3$/AlN and $CrCl_3$/AlN HSs. However, the supercell modeling of the CrI_3/AlN HSs contains >100 atoms, which makes the first-principles phonon calculations unfeasible with the limited computing resources.

The MCA energy (E_{MCA}) induced by the spin-orbit coupling (SOC) is evaluated based on the total energy difference between in-plane [100] and out-of-plane [001] magnetization directions, i.e., $E_{\mathrm{MCA}} = E_{[100]} - E_{[001]}$. Thus, the positive (negative) values of E_{MCA} denote an out-of-plane (in-plane) magnetic easy axis. The magnetic shape anisotropy (MSA) energy (E_{MSA}) originating from long-range magnetic dipole-dipole interactions is also considered via $E_{\mathrm{MSA}} = E^{\mathrm{Dipole}}_{[100]} - E^{\mathrm{Dipole}}_{[001]}$, where E^{Dipole} is calculated by

$$E^{\mathrm{Dipole}} = -\frac{1}{2}\frac{\mu_0}{4\pi}\sum_{i,j,i\neq j}\left[\frac{\vec{S}_i\cdot\vec{S}_j}{|\vec{r}_{ij}|^3} - \frac{3(\vec{S}_i\cdot\vec{r}_{ij})(\vec{S}_j\cdot\vec{r}_{ij})}{|\vec{r}_{ij}|^5}\right]. \quad (1)$$

Here, $\vec{S}_i$ is the local magnetic moment, and $\vec{r}_{ij}$ is the vector connecting sites i and j [53]. The calculations of Eq. (1) are carried out in the range of $\vec{r}_{ij} < 1000$ Å to ensure numerical reliability. It is worthwhile noting that the magnetic anisotropy energy (E_{MAE}) is essentially contributed by the two main terms, i.e., $E_{\mathrm{MAE}} = E_{\mathrm{MCA}} + E_{\mathrm{MSA}}$.

Here, T_c of the considered systems are obtained by Monte Carlo (MC) simulations based on a 2D Heisenberg model, which is described by the following Hamiltonian:

$$H = -J_1\sum_{ij}\vec{S}_i\cdot\vec{S}_j - J_2\sum_{ik}\vec{S}_i\cdot\vec{S}_k - J_3\sum_{il}\vec{S}_i\cdot\vec{S}_l - A_i\sum_i\left(\vec{S}_i^z\right)^2, \quad (2)$$

where J_1, J_2, and J_3 represent the first-, second-, and third-nearest-neighbor exchange interactions, respectively, A_i is the onsite single-ion anisotropy (SIA), and $\vec{S}_i^z$ is the z component of the spin vector. The four spin configurations used to calculate J_i ($i = 1, 2, 3$) and their corresponding energies are shown in Fig. S1 in the Supplemental Material [46]. The SIA is evaluated by using the four-state energy mapping method as described in Ref. [54]. The spin wave gap of the structures can be obtained based on linear spin wave theory [55], where the spin wave gap is given by $\Delta_0 = 2AS$ (without the inclusion of other anisotropic terms such as anisotropic exchange). The MC simulations are carried out on a hexagonal 100×100 lattice with periodic boundary conditions. Here, 10^5 MC steps are performed to equilibrate the system, and another

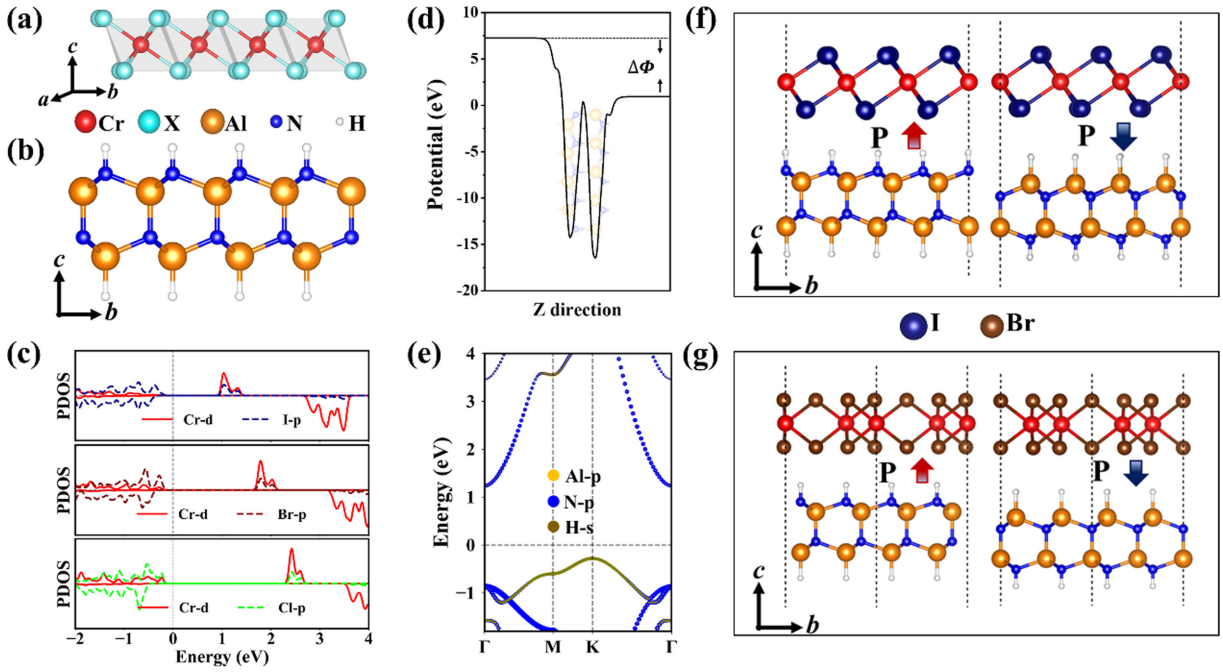

FIG. 1. Atomic structures and electronic properties of CrX_3 (X = I, Br, Cl) monolayers (MLs) and AlN bilayer (2L). (a) Side view of the atomic structure of a CrX_3 ML. (b) Side view of the fully hydrogenated AlN-2L. (c) Spin-polarized partial density of states (PDOS) of the CrX_3 ML. (d) The average electrostatic potential distribution of freestanding AlN-2L. $\Delta\Phi$ is the electrostatic potential difference defined as the energy difference of electrostatic potential between two sides of AlN-2L. (e) Projected band structure of the fully hydrogenated AlN-2L. Stacking configurations of CrX_3/AlN heterostructures (CrX_3 HS). (f) Side views of the most stable stacking configuration for CrI_3 HS. (g) Side views of the most stable stacking configuration for $CrBr_3$ HS.

10^7 MC steps per site are used for statistical averaging at each temperature.

III. RESULTS AND DISCUSSION

A. Electronic and magnetic properties of CrX_3 MLs

The CrX_3 (X = I, Br, Cl) MLs share similar crystal structures with the D_{3d} point group, in which the Cr layer is sandwiched by two X layers, and each Cr atom is surrounded by six X ligand atoms with an octahedral configuration [see Fig. 1(a)]. The near 90° Cr-X-Cr bonding angles lead to the dominating FM superexchange coupling within each ML, following the Goodenough-Kanamori-Anderson rules [56,57]. The calculated lattice parameters of CrI_3, $CrBr_3$, and $CrCl_3$ are 7.08, 6.50, and 6.11 Å, respectively, which agree well with previous reports [16,58,59]. Figure 1(c) displays the partial projected density of states (PDOS) of CrX_3 MLs. All CrX_3 MLs are semiconductors with bandgaps of 1.20, 1.94, and 2.59 eV for CrI_3, $CrBr_3$, and $CrCl_3$, respectively. The valence band maxima (VBM) are mainly contributed by X-p states, and the conduction band minima (CBM) are dominated by Cr-d states (also see the band structures in Fig. S2 in the Supplemental Material [46]), which are in accordance with previous calculations [16,17,30].

The calculated magnetic moment is ~3 μ_B in CrX_3 MLs, suggesting that the Cr atom adopts $S = \frac{3}{2}$ in the ground state. As expected, the MLs of CrX_3 all show ferromagnetism, featuring dominating J_1 (see Table I). Here, J_2 also prefers FM ordering, while J_3 is close to zero and thus negligible. The exchange parameters of CrX_3 MLs are comparable with previous studies [14,16,58]. The calculated SIA and spin wave gap of CrX_3 MLs are shown in Table S2 in the Supplemental Material [46]. The 0.527 meV spin wave gap of a CrI_3 ML is comparable with the inelastic neutron scattering observation (~0.4 meV) [60]. Based on J_i and SIA values, our MC simulations find that the resulting T_C for the pristine CrX_3 MLs are also in good agreement with their corresponding experimental values (see Table I) [1,12,13].

As presented in Table I, the calculated MCAs for CrX_3 MLs are all positive and monotonically decrease from I, Br to Cl, in good agreement with previous theoretical results [14,16,17]. In contrast, their MSAs are all negative. As a combined effect, the net MAE is positive for CrI_3 and $CrBr_3$ MLs but is negative for the $CrCl_3$ ML. This indicates that CrI_3 and $CrBr_3$ MLs have out-of-plane magnetic easy axes, while the $CrCl_3$ ML has an in-plane magnetic easy axis, which are perfectly consistent with the experimental observations [1,10–12]. The puzzling in-plane magnetic easy axis of the $CrCl_3$ ML compared with CrI_3 and $CrBr_3$ MLs can thus be ascribed to its in-plane MSA that dominates over its weak out-of-plane MCA [16].

B. Electronic and magnetic properties of CrX_3/AlN HSs

The crystal structure of hydrogenated a AlN-2L structure is shown in Fig. 1(b). The calculated in-plane lattice constant of AlN-2L is 3.08 Å. Due to the lack of inversion symmetry, the AlN-2L possesses an intrinsic spontaneous out-of-plane polarization with an electric dipole of 0.37 eÅ. As shown in Fig. 1(d), there is a potential drop ($\Delta\Phi$) of 6.37 eV across

TABLE I. Calculated lattice parameters (a) of freestanding CrX_3 ML, AlN-2L, and CrX_3/AlN HS, equilibrium interface distance (d), bandgap (E_g), number of electrons transferred between layers (ΔQ), magnetocrystalline anisotropy (MCA), magnetic shape anisotropy (MSA), exchange interaction parameters (J_n), and Curie temperatures (T_C).

Structures	a (Å)	d (Å)	E_g (eV)	ΔQ (e)	MCA (μeV/Cr)	MSA (μeV/Cr)	J_1 (meV)	J_2 (meV)	J_3 (meV)	T_C (K)
AlN-2L	3.08	—	1.52	—	—	—	—	—	—	—
CrI_3	7.08	—	1.20	—	768.3	−39.44	3.66	0.52	−0.02	45
CrI_3-HS-P ↑	12.29	2.53	0.00	0.82	−1070.8	−39.88	3.92	0.51	0.57	53
CrI_3-HS-P ↓	12.29	2.83	0.08	−0.03	1043.7	−37.36	4.25	0.45	−0.05	43
$CrBr_3$	6.50	—	1.94	—	164.5	−45.09	2.90	0.27	−0.03	24
$CrBr_3$-HS-P ↑	6.50	2.38	0.00	0.22	−604.4	−48.77	3.36	0.25	0.53	36
$CrBr_3$-HS-P ↓	6.50	2.72	0.90	0.02	148.2	−45.25	3.24	0.26	−0.02	28
$CrCl_3$	6.11	—	2.59	—	27.0	−50.49	2.26	0.15	−0.03	14
$CrCl_3$-HS-P ↑	6.11	2.32	0.00	0.25	−450.3	−54.95	2.14	0.16	0.46	22
$CrCl_3$-HS-P ↓	6.11	2.78	1.60	0.02	34.6	−49.32	2.36	0.12	−0.04	16

the two sides of the AlN-2L. The projected band structure of the AlN-2L is shown in Fig. 1(e), indicating that the AlN-2L is an indirect bandgap semiconductor with the VBM (CBM) dominated by H-s (N-p) orbitals.

With the asymmetric polar AlN-2L, two types of CrX_3/AlN HSs are constructed by placing the CrX_3 layer on the AlN-2L. One is formed with the polarization of the AlN-2L pointing away from the magnetic layer (denoted as CrX_3-HS-P ↓), and the other one has the polarization of the AlN-2L pointing toward the magnetic layer (denoted as CrX_3-HS-P ↑). A $\sqrt{3}\times\sqrt{3}$ CrI_3 ML and a 4×4 AlN layer are used to construct the CrI_3/AlN HS with a small lattice mismatch of only 0.3% exerted on AlN. When constructing $CrBr_3$/AlN and $CrCl_3$/AlN HSs, a 1×1 CrX_3 ML and a 2×2 AlN layer are adopted, and their corresponding mismatches are 5.4 and 0.8%, respectively. To exclude the strain effect on the magnetic properties of CrX_3 MLs, the strain from the lattice mismatch is completely exerted on the AlN-2L in constructing all CrX_3/AlN HSs. This is reasonable, as the polarization of the AlN-2L changes very little under a biaxial strain. For example, the electric dipole is 0.37 eÅ under 5% compressive strain and 0.35 eÅ under 5% tensile strain, and the global band structure of the AlN-2L also barely changes under the external strain (see Fig. S3 in the Supplemental Material [46]).

Two (three) representative stacking configurations are calculated to identify the energetically favorable configuration of CrI_3 HS ($CrBr_3$ HS and $CrCl_3$ HS), considering the symmetry of the CrX_3 ML and the AlN-2L, as shown in Fig. S4(a) in the Supplemental Material [46]. The relative total energies of the HSs with different stacking configurations are displayed in Fig. S4(b) in the Supplemental Material [46] for both the up and down electric polarization. The T0 configuration has the lowest energy for both CrI_3-HS-P ↑ and CrI_3-HS-P ↓, while for $CrBr_3$-HS-P ↑ ($CrBr_3$-HS-P ↓) and $CrCl_3$-HS-P ↑ ($CrCl_3$-HS-P ↓), the T1 (T2) is the most energetically favorable configuration. The corresponding side views of those configurations are shown in Figs. 1(f) and 1(g), respectively. All the results reported below for the HSs are calculated using the most stable structures. The thermodynamical stability of these HSs is demonstrated by our *ab initio* molecular dynamics simulations (see Fig. S5 in the Supplemental Material [46]). As shown in Fig. S6 in the Supplemental Material [46], no imaginary frequency presents in the whole Brillouin zone, indicating that the considered systems are dynamically stable. The interlayer distances are given in Table I. Here, CrX_3-HS-P ↑ has relatively smaller interlayer distance compared with CrX_3-HS-P ↓. This suggests the stronger interfacial interactions when the polarization is pointing toward the CrX_3 layer, which is also consistent with the fact that the binding energies in CrX_3-HS-P ↑ are larger than those in the CrX_3-HS-P ↓ ones.

We now investigate the respective physical origins of the interfacial interactions in these systems, which are the keys for understanding how the electronic and magnetic properties of CrX_3 MLs are affected when the HS is formed. Compared with the electronic states of the isolated CrX_3 MLs and the AlN-2L, which all are semiconductors, the Fermi level crosses the spin-up channel of CrX_3 MLs as well as some valence bands of the AlN-2L, resulting in a half-metallic state in CrX_3-HS-P ↑ (see Figs. 2(a), 3(a), and S7(a) in the Supplemental Material [46]). In contrast, the electronic structures behave quite differently in the case of CrX_3-HS-P ↓. They remain with semiconducting character with reduced bandgaps of 0.08, 0.90, and 1.60 eV for X = I, Br, and Cl, respectively (see Figs. 2(d), 3(d), and S7(d) in the Supplemental Material [46]). Therefore, a transition between semiconductor and half-metal in CrX_3/AlN HSs can be induced when the electric polarization direction of the AlN-2L is switched from down to up.

To understand the distinct electronic behaviors of CrX_3 with different electric polarization directions of the AlN-2L, we first check the band alignments of the CrX_3 HS to get the overall charge transfer trend when forming the HSs. The schematic diagrams of relative band edge positions with respect to the vacuum level are presented in Figs. 2(b), 2(e), 3(b), 3(e), S7(b), and S7(e) in the Supplemental Material [46]. Here, we take the CrI_3 HS as an example. When the polarization is upward, the bands of CrI_3 are brought so low that its local CBM lies lower than the local VBM of the AlN-2L. Therefore, electrons are allowed to transfer from the AlN-2L to the CrI_3 layer [see Fig. 2(b)]. Moreover, the planar averaged plot of its charge transfer is also shown in Fig. 2(c). Clearly, the transferred charges to the CrI_3 layer mostly distribute in the interfacial region, while the charge

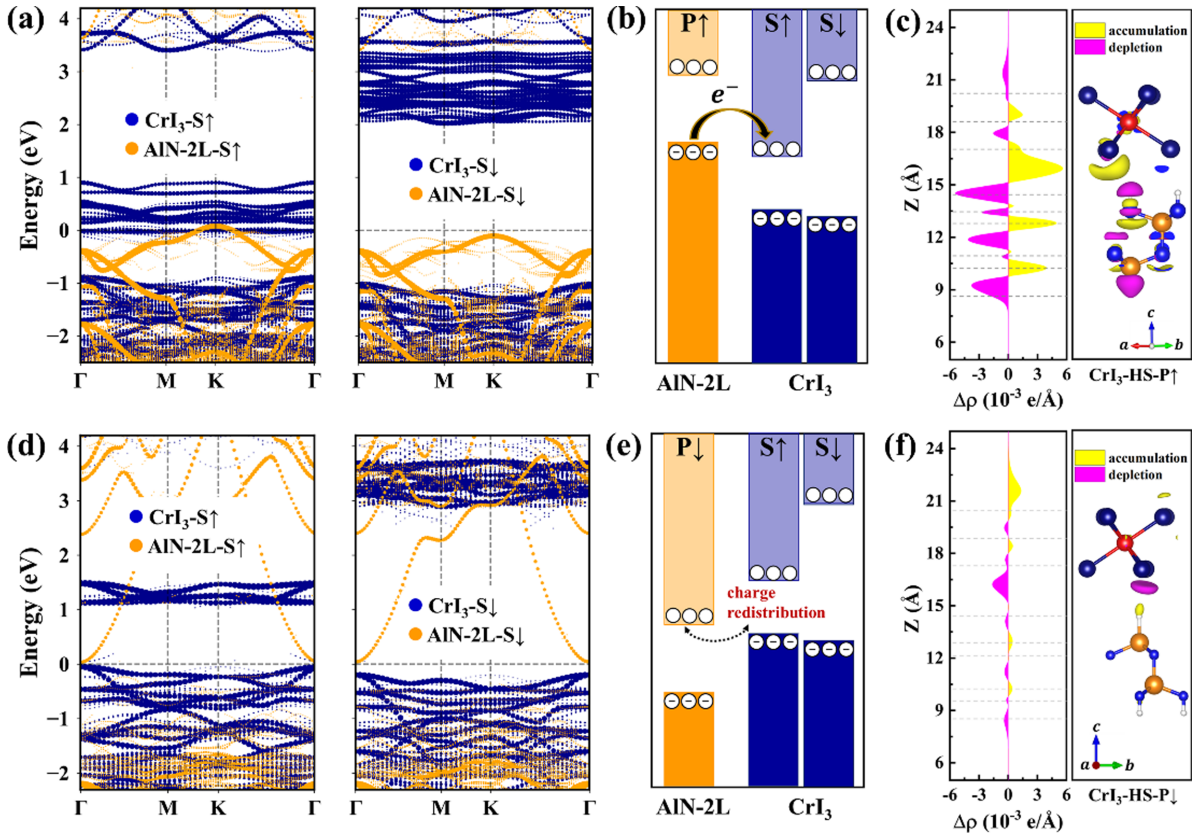

FIG. 2. Projected band structure of (a) CrI_3-HS-P ↑ and (d) CrI_3-HS-P ↓. Band alignments of (b) CrI_3-HS-P ↑ and (e) CrI_3-HS-P ↓ with respect to the vacuum level. S↑ and S↓ represent the spin-up and spin-down channels, respectively. Planar integrated and differential charge density of (c) CrI_3-HS-P ↑ and (f) CrI_3-HS-P ↓.

depletion is across the whole AlN layer. The electron doping of CrI_3 from the AlN layer leads to the partial occupation of the upper subset of Cr-3d orbitals, and a half-metallic state is thus induced in CrI_3-HS-P ↑. Similar behaviors are also observed in $CrBr_3$-HS-P ↑ [see Figs. 3(b) and 3(c)] and $CrCl_3$-HS-P ↑ (see Figs. S7(b) and S7(c) in the Supplemental Material [46]) cases. In contrast, when the polarization is downward, the band alignment in the HSs changes from the zero gap type-III to type-II (see Figs. 2(e), 3(e), and S7(e) in the Supplemental Material [46]), and the electrons thus cannot transfer efficiently between CrX_3 MLs and the AlN-2L and just slightly redistribute in these HSs (see Figs. 2(f), 3(f), and S7(f) in the Supplemental Material [46]). Consequently, the CrX_3 MLs in CrX_3-HS-P ↓ HSs retain their intrinsic semiconducting character. The electrons transferred between the CrX_3 and AlN layers (ΔQ) in the HSs are also obtained by the Bader charge analysis. A positive (negative) value indicates excess (deficiency) of electrons in the CrX_3 layer. As shown in Table I, the amounts of the transferred charges further confirm the above statements. The distinctly different band shifts of CrX_3 MLs when contacting with opposite sides of the AlN-2L arise from the inherent electric polarization of the AlN-2L. Especially the half-metallicity in CrX_3 MLs is highly desirable for their practical applications in nanospintronic devices, such as magnetic tunnel junctions, spin valves, or spin-effect transistors.

The magnetic properties, such as the exchange interactions and MCA of CrX_3/AlN HSs could also be modified by the distinct change of electronic structures with upward and downward electric polarization. For instance, in CrX_3-HS-P ↑, ferromagnetism is slightly enhanced due to the electron transferred from the AlN-2L to the CrX_3 layers. Such an enhancement is reflected in the calculated exchange parameters $J_{1,2,3}$ and increased magnetic moments of Cr ions (see Table S3 and Supplemental Note 2 in the Supplemental Material [46]). As a result, an increase of T_C by ∼10 K is observed relative to their corresponding pristine MLs (see Table I and Fig. S16 in the Supplemental Material [46]). The change of magnetization and T_C in CrX_3-HS-P ↓ is limited compared with their isolated MLs considering the weak vdW interlayer interactions. Meanwhile, FM order within the CrX_3 layers is preserved in all CrX_3/AlN HSs studied here (as seen in the dominated FM J_1 in Table I).

C. Origin of the tunable MCA in CrX_3/AlN HSs

We now explore how the MAEs of CrX_3 MLs are modulated by the interfacial coupling with the asymmetric polar AlN-2L nanosheets. The MAEs of CrX_3/AlN HSs are also summarized in Table I. It is interesting to note that, when stacked on AlN-2L-P ↓, the MCA of CrI_3 largely increases to 1043.7 μeV/Cr. However, the MCAs of the FM layers in $CrBr_3$-HS-P ↓ and $CrCl_3$-HS-P ↓ only change slightly with respect to their freestanding forms. When the dipole moment of the AlN-2L is switched to the upward direction, the MCAs for all the CrX_3-HS-P ↑ change to large negative values,

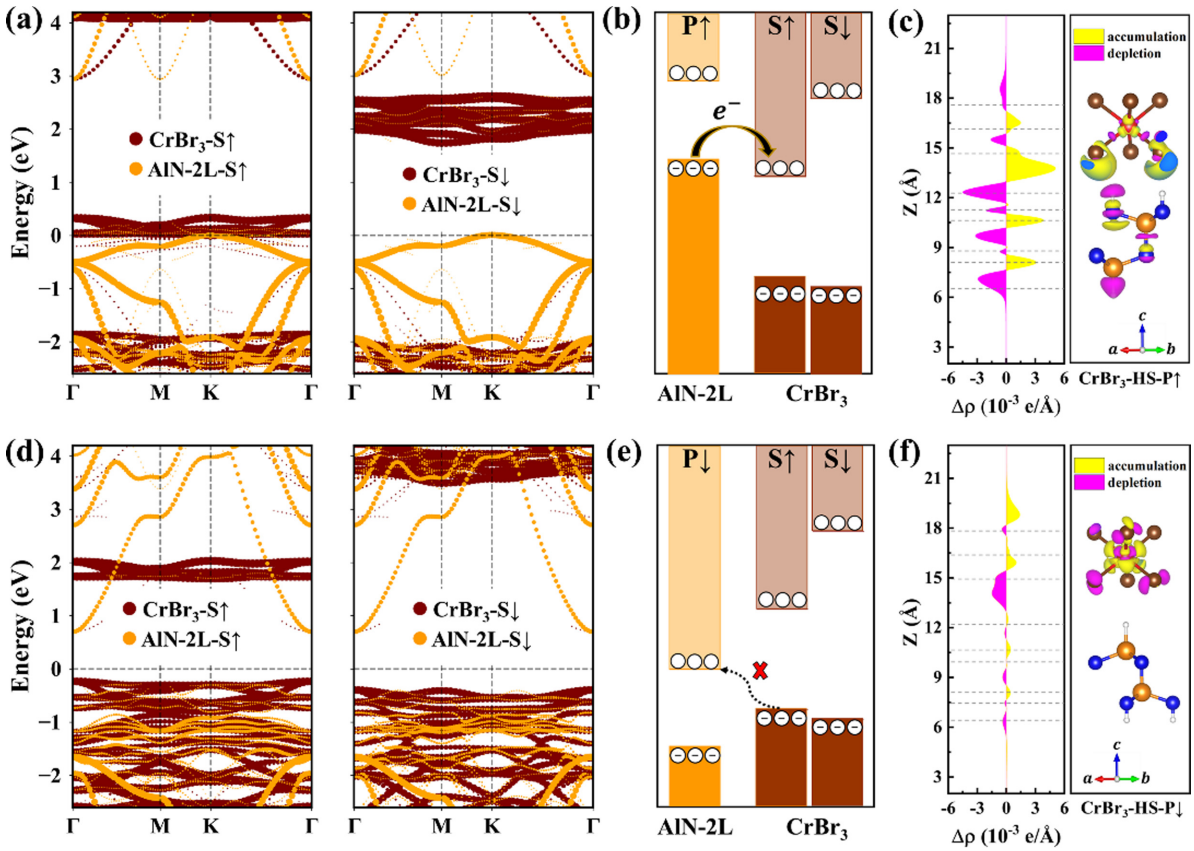

FIG. 3. Projected band structure of (a) $CrBr_3$-HS-P ↑ and (d) $CrBr_3$-HS-P ↓. Band alignments of (b) $CrBr_3$-HS-P ↑ and (e) $CrBr_3$-HS-P ↓ with respect to the vacuum level. S↑ and S↓ represent the spin-up and spin-down channels, respectively. Planar integrated and differential charge density of (c) $CrBr_3$-HS-P ↑ and (f) $CrBr_3$-HS-P ↓.

−1070.8, −604.4, and −450.3 μeV/Cr for X = I, Br, and Cl, respectively. This indicates that the CrX_3 MLs in CrX_3-HS-P ↑ favor an in-plane alignment of magnetization, in sharp contrast with the isolated CrX_3 MLs. On the other hand, the MSAs for all the systems remain negative, and the magnitudes are very close to each other upon polarization reversal. These results suggest that the MCA of 2D magnetic materials can be significantly tuned by integration into HSs with suitable polar layers. The remarkably enhanced out-of-plane MCA of CrI_3 on AlN-2L-P ↓ and the switchable magnetic easy axis of CrI_3 and $CrBr_3$ MLs with different electric polarization directions are important for their potential applications in spintronic devices.

To further understand the polarization regulation mechanism of the MCA in CrX_3 MLs on the AlN-2L, we proceed to inspect the details in their electronic structures, particularly the charge distribution and the accompanied changes of electron occupation in Cr-3d orbitals and X-p orbitals, which are expected to play key roles for the modulated magnetic properties in CrX_3 MLs. It is worth mentioning that our calculations indicate that the small structural changes of CrX_3 MLs on the AlN-2L have little impact on their MCAs. Here, we first consider the electronic structures of the isolated ML counterparts with the same crystal structures as in the corresponding HSs (denoted by CrX_3 MLs*-↑ and CrX_3 MLs*-↓). The atomic orbital projected band structure of CrI_3 ML*-↑ with SOC has been presented in Fig. S8 in the Supplemental Material [46]. The lowest states that would be occupied by the excess electrons are mainly related to Cr-$d_{xz/yz}$ and $d_{x^2-y^2/xy}$, hybridized with I-p orbitals. We also find that the main unquenched orbital angular momenta around the CBM of CrI_3 ML*-↑ are Cr L_z and I $L_{x/y}$, which are shown in Figs. 4(a) and 4(b), respectively. The orbital resolved MCAs on Cr and I atoms in CrI_3 ML*-↑ and CrI_3-HS-P ↑ are further compared in Figs. 4(c) and 4(d), respectively. The largest differences in the orbital resolved MCA in the two structures are associated with the orbital pairs of Cr ($d_{x^2-y^2}$, d_{xy}), Cr (d_{xz}, d_{yz}), I (p_x, p_y), and I ($p_{x/y}$, p_z). The larger enhanced negative contribution from I ($p_{x/y}$, p_z) (manifested by $\langle p_{x/y}|\hat{L}_x|p_z\rangle$) counteracts the smaller positive contributions from the Cr ($d_{x^2-y^2}$, d_{xy}) and I (p_x, p_y), which thus leads to the overall in-plane MCA in CrI_3-HS-P ↑. Similar analyses are also performed for $CrBr_3$ and $CrCl_3$ MLs (see Figs. S9–S11 in the Supplemental Material [46]). It is found that the electron doping when interfacing with P ↑ AlN-2L also contributes to an overall negative MCA in $CrBr_3$-HS-P ↑ and $CrCl_3$-HS-P ↑. Note that, in contrast to CrI_3 and $CrBr_3$ MLs, the MCA changes between $CrCl_3$ ML*-↑ and $CrCl_3$-HS-P ↑ are generally small (see Fig. S11 in the Supplemental Material [46] and Table I), mainly due to the weakening SOC from I, Br to Cl.

For CrI_3-HS-P ↓, the electron deficiency due to the charge redistribution across the interface indicates electron removal

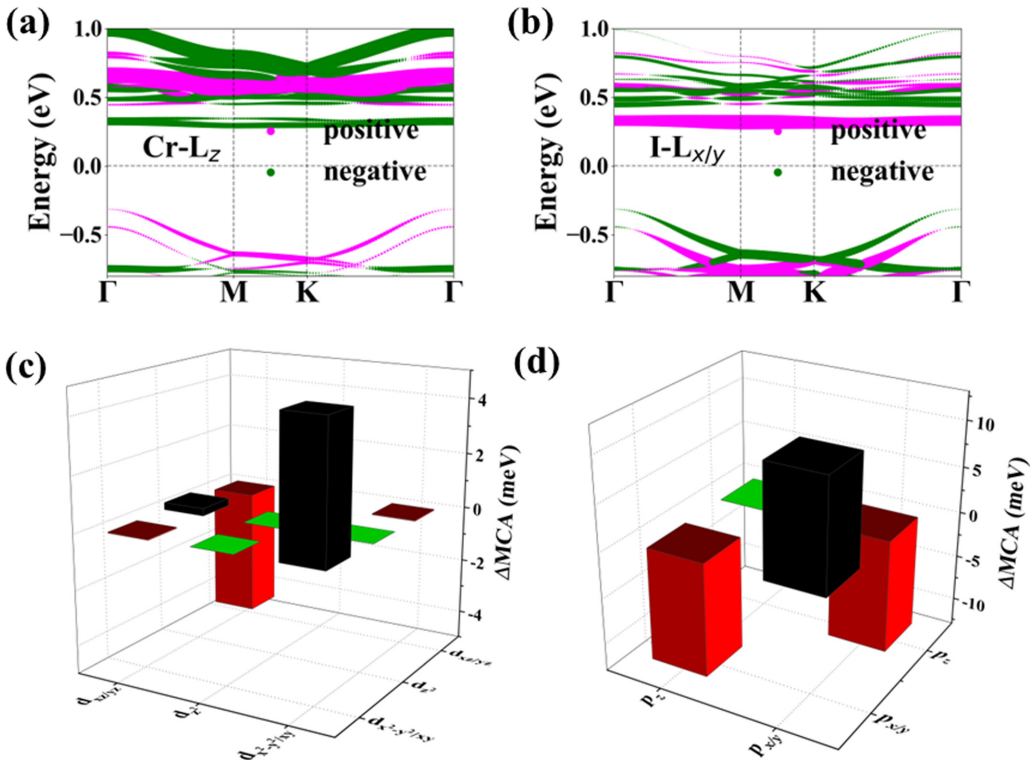

FIG. 4. Projections of orbital angular momentum L_z (a) from Cr atoms and (b) $L_{x/y}$ from I atoms in CrI_3 layer with its crystal structure from the HS-P ↑ case (CrI_3 ML*-↑). The size of the solid circles indicates the relative magnitude of each projection in the band structures in (a) and (b). Orbital resolved change in magnetocrystalline anisotropy (ΔMCA) of (c) Cr atoms and (d) I atoms between CrI_3 ML*-↑ and CrI_3-HS-P ↑.

from the top valence bands of the CrI_3 layer, which mainly consist of I-$p_{x/y}$ orbitals (see Fig. S12 in the Supplemental Material [46]). Since the occupied Cr-3d orbital-derived states are mostly well below the Fermi level, the MCA difference between isolated CrI_3 ML*-↓ and CrI_3-HS-P ↓ is mainly contributed by I atoms. As shown in Fig. 5(b), the I-$p_{x/y}$ orbitals at the valence band edge can give sizeable unquenched orbital momentum L_z (manifested by $\langle p_x|\hat{L}_z|p_y\rangle$), which thus contributes a large positive MCA given the strong SOC of I atoms. The orbital resolved MCA energy difference (ΔMCA) between CrI_3 MLs*-↓ and CrI_3-HS-P ↓ are shown in Figs. 5(c) and 5(d), respectively. It clearly indicates that the overall enhanced positive MCA in CrI_3-HS-P ↓ mainly results from the orbital pair of I (p_x, p_y) through $\hat{L}_z$ for the slightly p-doped CrI_3 layer, while the MCA contributions of Cr from the d orbitals are almost unchanged. The situation is different for $CrBr_3$-HS-P ↓ and $CrCl_3$-HS-P ↓, where there is no electron deficiency due to the large offsets in the band alignments (see Figs. 3(e) and S7(e) in the Supplemental Material [46]). As a result, their MCAs are close to that of the isolated $CrBr_3$ and $CrCl_3$ MLs (see Figs. S13–S15 in the Supplemental Material [46]).

Overall, constructing HSs with CrX_3 (X = I, Br, Cl) MLs and a polar layer proves to be an effective way to realize the tuning of their MCAs. However, the choice of the polar constituent is constrained, as discussed below. To enhance the out-of-plane MCAs of CrX_3, suitable polar layers should have their CBM extremely close to or even lower than the VBM of CrX_3 (i.e., electron deficiency for CrX_3 MLs). This is particularly true for CrI_3 and $CrBr_3$, since their VBM states are composed of I- and Br-p orbitals with strong SOCs. To verify this, we calculate the MCA of the isolated CrI_3 ML with identical electrons removed as in CrI_3-HS-P ↓. As expected, an obviously enhanced MCA (992.6 μeV/Cr) is obtained. When the dipole direction of the polar layer is reversed and pointing toward the CrX_3 MLs, the inherent dipole field will bring down the CBM of CrX_3 MLs lower than the VBM of the polar layer (i.e., electron excess for CrX_3 MLs). Accordingly, the in-plane MCAs of CrX_3 layers are enhanced. Therefore, the MCAs of CrX_3 layers can be switched between in-plane and out-of-plane directions with suitable polar layers. Such wide tunable MCA via building 2D vdW HSs make the realization of energy-efficient spintronic devices possible. We further calculated the interlayer charge transfer and MCAs in CrX_3/AlN HSs with different configurations, as shown in Table S4 in the Supplemental Material [46]. These results suggest that the interlayer configuration has limited effect on the charge transfer and thus magnetic anisotropy.

IV. CONCLUSIONS

In conclusion, we systematically studied the tunability of electronic and magnetic properties of CrX_3 (X = I, Br, Cl) in assembled HSs with the polar AlN layer based on first-

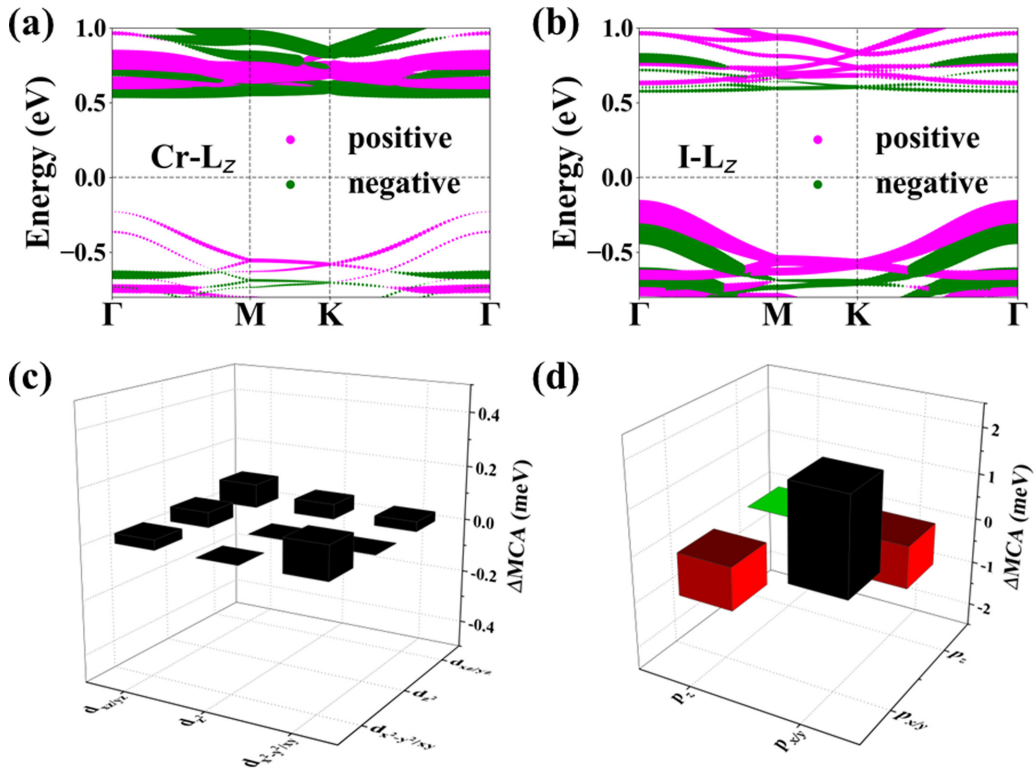

FIG. 5. Projections of orbital angular momentum (a) L_z from Cr atoms and (b) L_z from I atoms in CrI_3 layer with its crystal structure from HS-P ↓ case (CrI_3 ML*-↓). The size of the solid circles indicates the relative magnitude of each projection in the band structures in (a) and (b). Orbital resolved change in magnetocrystalline anisotropy (ΔMCA) of (c) Cr atoms and (d) I atoms between CrI_3 ML*-↓ and CrI_3-HS-P ↓.

principles DFT calculations. We find that the magnetic anisotropy of CrX_3 MLs in CrX_3/AlN HSs is switched between out-of-plane and in-plane directions by reversing the direction of the polar dipole field in the AlN layers. The underlying origin of the switchable magnetic anisotropy in these HSs is attributed to the charge transfer and redistribution between the constituent layers that are governed by the band alignments between CrX_3 and polar AlN layers. Meanwhile, our results of CrX_3-HP-P ↑ HSs suggest a practical approach to achieve half-metallicity in CrX_3 layers and boost their Curie temperatures. In this paper, we demonstrate that assembling 2D magnetic materials into HSs with suitable polar layers provides an efficient and nonvolatile way to tune their electronic and magnetic properties, which can be of great use in future spintronics.

ACKNOWLEDGMENTS

This paper was supported by the National Natural Science Foundation of China under Grants No. 11774142, No. 12004160, and No. 12104518, the Shenzhen Basic Research Fund under Grant No. JCYJ20180504165817769, and the Open Project of Guangdong Provincial Key Laboratory of Magnetoelectric Physics and Devices under Grant No. 2020B1212060030. Computational time was supported by the Center for Computational Science and Engineering of Southern University of Science and Technology, and the Major Science and Technology Infrastructure Project of Material Genome Big-science Facilities Platform supported by Municipal Development and Reform Commission of Shenzhen.

[1] B. Huang, G. Clark, E. Navarro-Moratalla, D. R. Klein, R. Cheng, K. L. Seyler, D. Zhong, E. Schmidgall, M. A. McGuire, D. H. Cobden *et al.*, Nature (London) **546**, 270 (2017).
[2] C. Gong, L. Li, Z. Li, H. Ji, A. Stern, Y. Xia, T. Cao, W. Bao, C. Wang, Y. Wang *et al.*, Nature (London) **546**, 265 (2017).
[3] Y. Deng, Y. Yu, Y. Song, J. Zhang, N. Z. Wang, Z. Sun, Y. Yi, Y. Z. Wu, S. Wu, J. Zhu *et al.*, Nature (London) **563**, 94 (2018).
[4] N. D. Mermin and H. Wagner, Phys. Rev. Lett. **17**, 1307 (1966).
[5] C. Gong and X. Zhang, Science **363**, eaav4450 (2019).
[6] T. Song, X. Cai, M. W.-Y. Tu, X. Zhang, B. Huang, N. P. Wilson, K. L. Seyler, L. Zhu, T. Taniguchi, K. Watanabe *et al.*, Science **360**, 1214 (2018).
[7] H. H. Kim, B. Yang, T. Patel, F. Sfigakis, C. Li, S. Tian, H. Lei, and A. W. Tsen, Nano Lett. **18**, 4885 (2018).
[8] M. H. Kryder, Thin. Solid. Films **216**, 174 (1992).
[9] A. Prinz Gary, Science **282**, 1660 (1998).
[10] X. Cai, T. Song, N. P. Wilson, G. Clark, M. He, X. Zhang, T. Taniguchi, K. Watanabe, W. Yao, D. Xiao *et al.*, Nano Lett. **19**, 3993 (2019).
[11] H. H. Kim, B. Yang, S. Li, S. Jiang, C. Jin, Z. Tao, G. Nichols, F. Sfigakis, S. Zhong, C. Li *et al.*, Proc. Natl. Acad. Sci. USA **116**, 11131 (2019).
[12] Z. Zhang, J. Shang, C. Jiang, A. Rasmita, W. Gao, and T. Yu, Nano Lett. **19**, 3138 (2019).

[13] M. A. McGuire, G. Clark, Santosh KC, W. M. Chance, G. E. Jellison, Jr., V. R. Cooper, X. Xu, and B. C. Sales, Phys. Rev. Mater. **1**, 014001 (2017).
[14] L. Webster and J.-A. Yan, Phys. Rev. B **98**, 144411 (2018).
[15] C. Huang, J. Feng, F. Wu, D. Ahmed, B. Huang, H. Xiang, K. Deng, and E. Kan, J. Am. Chem. Soc. **140**, 11519 (2018).
[16] F. Xue, Y. S. Hou, Z. Wang, and R. Q. Wu, Phys. Rev. B **100**, 224429 (2019).
[17] J. Kim, K. W. Kim, B. Kim, C. J. Kang, D. Shin, S. H. Lee, B. C. Min, and N. Park, Nano Lett. **20**, 929 (2020).
[18] M. Luo and Y. H. Shen, JETP Lett. **112**, 58 (2020).
[19] F. Matsukura, Y. Tokura, and H. Ohno, Nat. Nanotechnol. **10**, 209 (2015).
[20] B. Huang, G. Clark, D. R. Klein, D. MacNeill, E. Navarro-Moratalla, K. L. Seyler, N. Wilson, M. A. McGuire, D. H. Cobden, D. Xiao *et al.*, Nat. Nanotechnol. **13**, 544 (2018).
[21] L. Ciorciaro, M. Kroner, K. Watanabe, T. Taniguchi, and A. Imamoglu, Phys. Rev. Lett. **124**, 197401 (2020).
[22] A. S. Ahmad, Y. Liang, M. Dong, X. Zhou, L. Fang, Y. Xia, J. Dai, X. Yan, X. Yu, J. Dai *et al.*, Nanoscale **12**, 22935 (2020).
[23] F. Xue, Z. Wang, Y. Hou, L. Gu, and R. Wu, Phys. Rev. B **101**, 184426 (2020).
[24] S. Shen, Q. Wu, Y. Dai, B. Huang, and Y. Ma, Phys. Rev. B **104**, 064446 (2021).
[25] C. Gong, E. M. Kim, Y. Wang, G. Lee, and X. Zhang, Nat. Commun. **10**, 2657 (2019).
[26] Y. Zhao, J.-J. Zhang, S. Yuan, and Z. Chen, Adv. Funct. Mater. **29**, 1901420 (2019).
[27] Y. Lu, R. Fei, X. Lu, L. Zhu, L. Wang, and L. Yang, ACS Appl. Mater. Interfaces **12**, 6243 (2020).
[28] G. Wang, W. Qin, S. Wang, B. S. Teketel, W. Yu, T. Luo, B. Xu, and B. Lin, ACS Appl. Mater. Interfaces **13**, 16694 (2021).
[29] M. Zhao, X. Dai, and Y. Tang, Phys. Chem. Chem. Phys. **22**, 20477 (2020).
[30] M. Yang, H. Shu, P. Tang, P. Liang, D. Cao, and X. Chen, ACS Appl. Mater. Interfaces **13**, 8764 (2021).
[31] Q.-F. Xu, W.-Q. Xie, Z.-W. Lu, and Y.-J. Zhao, Phys. Lett. A **384**, 126754 (2020).
[32] W.-n. Ren, K.-j. Jin, J.-s. Wang, C. Ge, E.-J. Guo, C. Ma, C. Wang, and X. Xu, Sci. Rep. **11**, 2744 (2021).
[33] H. Ye, X. Wang, D. Bai, J. Zhang, X. Wu, G. P. Zhang, and J. Wang, Phys. Rev. B **104**, 075433 (2021).
[34] S. Jiang, L. Li, Z. Wang, K. F. Mak, and J. Shan, Nat. Nanotechnol. **13**, 549 (2018).
[35] H. He, L. Huang, M. Xiao, Y. Fu, X. Shen, and J. Zeng, J. Mater. Sci. Mater. Electron. **24**, 4499 (2013).
[36] P. Tsipas, S. Kassavetis, D. Tsoutsou, E. Xenogiannopoulou, E. Golias, S. A. Giamini, C. Grazianetti, D. Chiappe, A. Molle, M. Fanciulli *et al.*, Appl. Phys. Lett. **103**, 251605 (2013).
[37] C. Bacaksiz, H. Sahin, H. D. Ozaydin, S. Horzum, R. T. Senger, and F. M. Peeters, Phys. Rev. B **91**, 085430 (2015).
[38] L. Li and M. Wu, ACS Nano **11**, 6382 (2017).
[39] M. Zhao, Y. Xia, X. Liu, Z. Tan, B. Huang, C. Song, and L. Mei, J. Phys. Chem. B **110**, 8764 (2006).
[40] W. Wang, Y. Zheng, X. Li, Y. Li, H. Zhao, L. Huang, Z. Yang, X. Zhang, and G. Li, Adv. Mater. **31**, 1803448 (2019).
[41] M. Beshkova and R. Yakimova, Vacuum **176**, 109231 (2020).
[42] A. Konishi, T. Ogawa, C. A. J. Fisher, A. Kuwabara, T. Shimizu, S. Yasui, M. Itoh, and H. Moriwake, Appl. Phys. Lett. **109**, 102903 (2016).
[43] G. Kresse and J. Furthmüller, Phys. Rev. B **54**, 11169 (1996).
[44] J. P. Perdew, K. Burke, and M. Ernzerhof, Phys. Rev. Lett. **77**, 3865 (1996).
[45] P. E. Blöchl, Phys. Rev. B **50**, 17953 (1994).
[46] See Supplemental Material at http://link.aps.org/supplemental/10.1103/PhysRevB.106.134412 for more details on the structure and electronic and magnetic results and Refs. [16,24,61–63].
[47] V. I. Anisimov, F. Aryasetiawan, and A. I. Lichtenstein, J. Phys. Condens. Matter **9**, 767 (1997).
[48] S. L. Dudarev, G. A. Botton, S. Y. Savrasov, C. J. Humphreys, and A. P. Sutton, Phys. Rev. B **57**, 1505 (1998).
[49] H. J. Monkhorst and J. D. Pack, Phys. Rev. B **13**, 5188 (1976).
[50] S. Grimme, J. Comput. Chem. **27**, 1787 (2006).
[51] T. Bučko, J. Hafner, S. Lebègue, and J. G. Ángyán, J. Phys. Chem. A **114**, 11814 (2010).
[52] A. Togo and I. Tanaka, Scr. Mater. **108**, 1 (2015).
[53] J. D. Jackson, *Classical Electrodynamics*, 3rd ed. (Wiley, New York, 1998).
[54] H. Xiang, C. Lee, H.-J. Koo, X. Gong, and M.-H. Whangbo, Dalton Trans. **42**, 823 (2013).
[55] S. Toth and B. Lake, J. Phys.: Condens. Matter **27**, 166002 (2015).
[56] P. W. Anderson, Phys. Rev. **79**, 350 (1950).
[57] J. Kanamori, J. Phys. Chem. Solids **10**, 87 (1959).
[58] W.-B. Zhang, Q. Qu, P. Zhu, and C.-H. Lam, J. Mater. Chem. C **3**, 12457 (2015).
[59] S. Tomar, B. Ghosh, S. Mardanya, P. Rastogi, B. S. Bhadoria, Y. S. Chauhan, A. Agarwal, and S. Bhowmick, J. Magn. Magn. Mater **489**, 165384 (2019).
[60] L. Chen, J.-H. Chung, T. Chen, C. Duan, A. Schneidewind, I. Radelytskyi, D. J. Voneshen, R. A. Ewings, M. B. Stone, A. I. Kolesnikov *et al.*, Phys. Rev. B **101**, 134418 (2020).
[61] N. Sivadas, S. Okamoto, X. D. Xu, C. J. Fennie, and D. Xiao, Nano Lett. **18**, 7658 (2018).
[62] A. V. Kuklin, M. A. Visotin, W. Baek, and P. V. Avramov, Physica E **123**, 114205 (2020).
[63] S. W. Jang, M. Y. Jeong, H. Yoon, S. Ryee, and M. J. Han, Phys. Rev. Mater. **3**, 031001(R) (2019).